iScience

CellPress
OPEN ACCESS

Article

Limits of dropwise condensation heat transfer on dry nonwetting surfaces

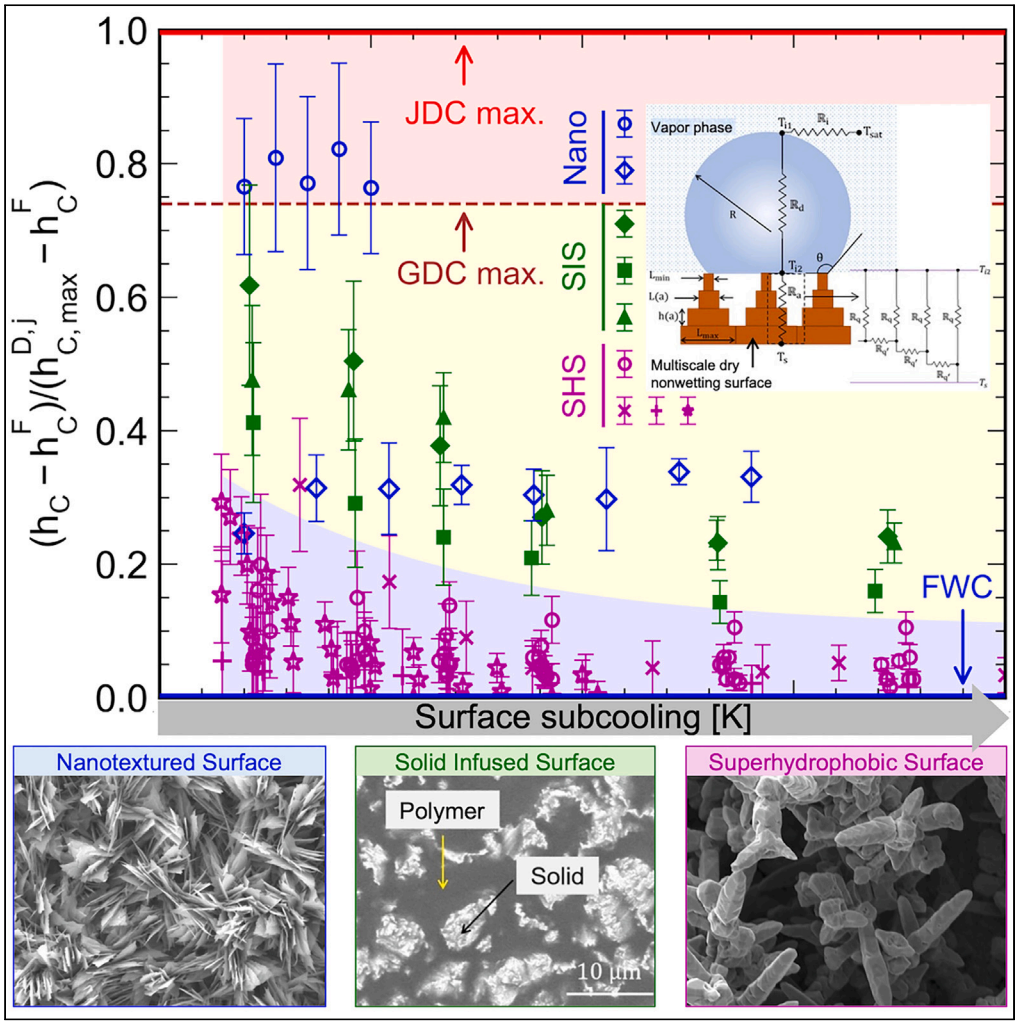

Sandeep Hatte, Ranga Pitchumani

pitchu@vt.edu

Highlights

Presents upper limit for condensation heat transfer on dry nonwetting surfaces

Theoretical upper limit considers different condensation modes in a unified manner

Data on several nonwetting surfaces from various studies compared with the bounds

Theoretical upper bound provides opportunity gap for future materials innovation

Hatte & Pitchumani, iScience *27*, 111059
November 15, 2024
https://doi.org/10.1016/j.isci.2024.111059

iScience

CellPress
OPEN ACCESS

Article

Limits of dropwise condensation heat transfer on dry nonwetting surfaces

Sandeep Hatte[1] and Ranga Pitchumani[1,2,*]

SUMMARY

Surface condensation is ubiquitous in applications such as power generation and desalination. Nonwetting surfaces have been studied extensively for their dropwise condensation potential with reports of dramatic improvements relative to the classical Nusselt equation for film-wise condensation that has long served as a reference theoretical *lower bound* on the condensation heat transfer coefficient. However, a theoretical *upper bound* on the *maximum* possible condensation heat transfer over a given surface is not available. Considering actual surface topographies as fractal surfaces, we present theoretical upper bounds for gravity-driven and jumping droplet condensation modes in a unified manner. Experimental data on steam condensation from this study as well as the literature on dry nonwetting surfaces are compared to the bounds to identify the opportunity gap to the theoretical maximum. Solid-infused surfaces, introduced recently by the authors, are shown to fall in this opportunity space, closer to the upper bound.

INTRODUCTION

Nonwetting surfaces have attracted attention over the years for potential applications such as drag reduction,[1–5] phase change heat transfer,[6–11] convective heat transfer,[12–14] anti-icing,[15–17] and anti-fouling,[18–20] to name a few. The physicochemical properties that give rise to the characteristics of nonwetting surfaces are texturing of the surfaces to produce either ordered or random arrangement of asperity peaks and valleys, wettability of the bare surface, and the type of infusion material occupying the asperity valleys. Nonwetting surfaces with a liquid lubricant as the infusion material are termed lubricant infused surfaces (LIS) that are distinguished from the nonwetting surfaces of present focus, with air or a solid as the inter-asperity material, which are collectively referred to as *dry nonwetting surfaces* (DNS) to include a broad class of hydrophobic (HS), superhydrophobic (SHS), and solid-infused surfaces (SIS).[20–22]

Superhydrophobic surfaces, due to the presence of air in the valleys of textured surfaces, offer much higher contact angle ($>150°$) and significantly lower contact angle hysteresis ($<5°$) compared to liquid or solid infused porous surfaces.[20–23] Condensation heat transfer over such surfaces results in the formation of spherical droplets that exhibit excellent mobility in contrast to the liquid condensate film that is often formed adherent on smooth non-structured hydrophilic surfaces.[19] It is the lower adhesion of condensate droplets to nonwetting surfaces that leads to enhanced condensation heat transfer performance as compared to film-wise condensation (FWC) where the condensate film remains in contact with the smooth surface for a longer time.

Several analytical,[24–26] experimental[7–9,27] or numeral studies[28] have been reported on dropwise condensation (DWC) on *monoscaled* micro- and/or nano-structured pillared superhydrophobic surfaces. Theoretical studies, in particular, have focused on the quasi-static mechanism of dropwise condensation and the resulting enhanced heat transfer rate attributed to the following process: condensate droplets of higher contact angle and lower contact angle hysteresis nucleate at random locations on the condensing surface and grow by direct vapor accumulation until they reach the size at which coalescence starts. In a phenomenon called jumping droplet condensation (JDC) that is observed on nanostructured surfaces under a limited range of subcooling and short durations, the drops are propelled away from the surface at the time of coalescence.[24,27] Coalescence-driven further growth of condensate droplets leads to shedding induced by gravity, called gravity-driven condensation (GDC). Both JDC and GDC result in droplet shedding at relatively smaller size compared to FWC. Early and more frequent shedding of smaller-sized condensate droplets leads to renewal of the surface for fresh nucleation at a higher rate, collectively leading to enhanced condensation heat transfer when compared to FWC. Considering the superhydrophobic surface to be an *idealized,* regularly-patterned, pillared asperity structure, existing models describe single droplet heat transfer rate on the surface. Further, through population balance, droplet size distribution theory and analytical formulation for maximum (departure) droplet size are developed, using which condensation heat transfer on structured superhydrophobic surfaces have been reported under the assumption of steady state for GDC and JDC modes of condensation.[24–26]

Unlike pillared nonwetting surfaces that are *monoscaled* structures with deterministic spacing, multiscale rough superhydrophobic surfaces have a statistical distribution of asperity sizes and spacings that span multiple scales. Figure 1 presents scanning electron micrographs

[1]Advanced Materials and Technologies Laboratory, Department of Mechanical Engineering, Virginia Tech, Blacksburg, VA 24061-0238, USA
[2]Lead contact
*Correspondence: pitchu@vt.edu
https://doi.org/10.1016/j.isci.2024.111059

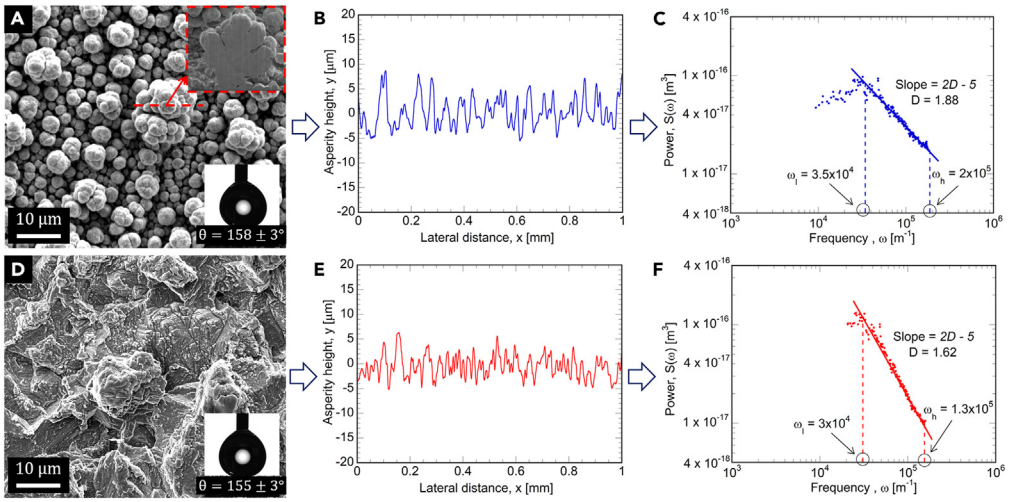

Figure 1. Fractal characterization of multiscale rough nonwetting surfaces

(A and D) SEM image, (B and E) profilometric scan and (C and F) power spectral density of (A–C) electrodeposited copper surface and (D–F) chemically etched copper surface. Scale bar size is 10 µm.

of superhydrophobic surfaces fabricated using electrodeposition or chemical etching, which clearly reveal *multiscaled* asperity topographies that cannot be represented by an ordered array of pillared structures. Further, the existing condensation models take into consideration the predictive wettability states of condensate droplets on prismatic pillared textures. However, such models cannot be extended for condensate droplets resting over multiscale rough surfaces. The resulting difference in the dynamics of contact angle and contact angle hysteresis, in turn, affects single droplet heat transfer characteristics, droplet size distribution and droplet departure during condensation, which are not accounted for in any of the previous studies. As a result, the existing theoretical description of condensation on regularly patterned superhydrophobic surfaces bears little applicability to studying condensation heat transfer on multiscale rough superhydrophobic surfaces fabricated using scalable processes in practice.

Toward addressing the fundamental knowledge gaps, here we present a detailed theoretical model for dropwise condensation over superhydrophobic rough surfaces by considering their inherent multiscale features during condensation. Multiscale rough surfaces are modeled as a fractal topography whose parameters are uniquely determined from surface profile scans. We present a unified model for heat transfer of a single condensate droplet resting on a fractal asperity network which incorporates the effects of the fractal surface parameters and surface subcooling. Further, the present model considers the two modes of condensate droplet shedding namely, gravity driven condensation (GDC) wherein droplet grow through coalescence until the force of gravity results in condensate shedding and secondly the jumping droplet condensation (JDC) in which the condensate droplets depart from the surface at the time of coalescence. A detailed droplet size distribution analysis is used to obtain closed-form analytical formulations for the maximum droplet size of the departing droplet in GDC and JDC modes of DWC and, in turn, the condensation heat transfer coefficient as function of the surface fractal parameters and subcooling.

The model considers the droplets to be in the Cassie state of wettability throughout the condensation process, thereby providing the *theoretical maximum* possible condensation heat transfer coefficients for GDC and JDC on the nonwetting surface. Together with the classical Nusselt correlation for FWC that yields the *lower* bound on the condensation heat transfer, the present study provides the theoretical *upper* bound for GDC and JDC on a given multiscale surface topography. Several designs of rough surfaces are parametrically analyzed to elucidate the influence of multiscale topography on condensation heat transfer enhancement. Experimental data from literature studies on GDC and JDC on monoscaled and multiscaled HS and SHS, as well as experimental measurements on GDC on electrodeposited and chemically etched HS and SHS in the present study, are pooled together to demonstrate their performance relative to the *lower* and the *upper* bounds. The gap between the range of heat transfer coefficients of the SHS that have been explored so far and the theoretical upper bounds is identified as the opportunity space for materials development. It is shown that solid-infused surface (SIS), a recent class of dry nonwetting surface introduced by the authors, significantly improves heat transfer approaching the performance of JDC on nanotextured surfaces and the *upper* bounds derived from the present model. The gap between the current performance of SIS and the theoretical upper bounds offers possibilities for future materials innovation.

RESULTS AND DISCUSSION

Fractal surface characterization

Multiscale rough surfaces exhibit asperities at a cascade of length scales ranging from micrometers to nanometers. Figures 1A and 1D show two scanning electron microscope (SEM) images of copper surfaces fabricated using electrodeposition and chemical etching, respectively.

The inset in Figure 1A is a focused ion beam cross section of a cauliflower-shaped asperity which reveals the distinct multiscale features. The presence of multiscale features on the surface is further evident from the profilometric scans shown in Figures 1B and 1E.

Such multiscale rough surfaces may be modeled using the Weierstrass-Mandelbrot (W-M) function,[29–31] which mathematically represents the self-similar structure of the surface profile scans as in Figures 1B and 1E. The Fourier transform of the W-M function yields a power-law dependence of the spectral density, $S(\omega)$, with the spatial frequency, ω, given by $S(\omega) = \frac{G^{2(D-1)}}{2\ln\gamma}\frac{1}{\omega^{5-2D}}$, where D and G are the fractal dimension and scaling constant, respectively, and $\gamma = 1.5$ represents the random phases in a roughness profile.[29,30] Similarly, the power spectral density of the actual multiscale rough surface may be obtained as a fast Fourier transform of the surface profile scans. By comparing the power spectra of the actual surface with that of the W-M function, we obtain the fractal dimension, D, and G of the multiscale rough surface.

Illustrating the method, Figures 1C and 1F show fast Fourier transformed power spectral density of the surface scans on the electrodeposited (Figure 1A) and chemically etched copper surfaces (Figure 1D), respectively, plotted on a log-log scale. Figures 1C and 1F reveal that in the range of spatial frequency, $\omega_\ell < \omega < \omega_h$, the power spectra, $S(\omega)$, follow power-law variation with spatial frequency as evident from the linear trend of the data points on the log-log plots. The power-law variation mathematically confirms the fractal nature of the multiscale rough surfaces, where the contributing spatial wavelengths of the surface profiles relate to the maximum and minimum length scales of the asperities, respectively, such that $L_{max} = \frac{1}{\omega_\ell}$ and $L_{min} = \frac{1}{\omega_h}$. From the values of minimum and maximum spatial frequencies shown in Figures 1C and 1F, the values of maximum and minimum asperity length scales are noted as follows: for the representative electrodeposited copper surface (Figure 1A), $L_{max} \approx 28\ \mu m$ and $L_{min} \approx 5\ \mu m$, for the etched rough surface (Figure 1D), $L_{max} \approx 33\ \mu m$ and $L_{min} \approx 8\ \mu m$.

Taking the logarithm of the power spectrum of the W-M function, $\log_{10}[S(\omega)] = -(5-2D)\cdot\log_{10}\omega + \log_{10}\left[\frac{G^{2(D-1)}}{2\ln\gamma}\right]$, and comparing it to the linear best fit through the data on the power spectrum plots in the range (ω_ℓ, ω_h), we see that (a) the slope of the best-fit line equals $2D - 5$, from which the fractal dimension, D, of the actual rough surface can be calculated, as seen in Figures 1C and 1D, where $D = 1.88$ and $D = 1.62$, for the representative electrodeposited and etched rough surfaces, respectively, and (b) the intercept of the best-fit line with the ordinate can be used to determine the scaling constant G of the multiscale surface, such that $G \approx 1.5\ \mu m$ and $G \approx 1.0\ \mu m$, for the electrodeposited and etched rough surfaces, respectively. The fractal parameters of the actual multiscale rough topography—D, G and asperity length scale ratio, $L^* = L_{max}/L_{min}$—are thus uniquely determined, which serve as the basis for further analysis.

In a fractal model of a real multiscale rough surface, the asperities are represented as a stack of prismatic structures each of square cross-sectional area, $a\ (= L^2)$, arranged one above another with length scales decreasing monotonically from L_{max} (bottommost asperity of area $a_{max} = L_{max}^2$) to L_{min} (topmost asperity of area $a_{min} = L_{min}^2$). Figure 2A depicts condensate droplets of varying sizes on a surface with multiscale asperity topography from which Figure 2B illustrates a close-up view of a single droplet resting on such a multiscale rough nonwetting surface. The surface temperature at the base of the multiscale asperities is T_s and the saturated steam surrounding the condensate droplet is at temperature, T_{sat}, which are both considered constant throughout, such that a constant surface subcooling is defined as $\Delta T = T_{sat} - T_s$. The height of each asperity is related to its cross-sectional area, a, in terms of the fractal parameters as $h(a) = a^{\left(1-\frac{D}{2}\right)}G^{D-1}$.[30,31] In a planar cross section of the fractal asperity structures, the number of asperities, N, with area, A, exceeding a is obtained in terms of fractal dimension D as $N(A \geq a) = \left(\frac{a}{a_{max}}\right)^{-\frac{D}{2}}$[27,28], from which the number of asperities with areas in the range a to $a + da$—the number density, $n(a)$—is obtained as $n(a) = -\frac{dN}{da} = \frac{D}{2a}\left(\frac{a_{max}}{a}\right)^{\frac{D}{2}}$. The fractal surface description and the associated parameters are used in the modeling of water contact angle on the surface, which is, in turn, used in the description of droplet size distribution and condensation heat transfer over multiscale rough surfaces.

Contact angle modeling

Condensation heat transfer over multiscale rough nonwetting surfaces is dependent on the contact angle and contact angle hysteresis that are, in turn, functions of the multiscale rough surface topography, surface functionalization and subcooling. In our previous work,[30] we developed a relationship between equilibrium contact angle, θ, and the fractal parameters of a multiscale surface as:

$$\cos\theta = \left(\frac{D}{D-2}\right)\left(\frac{L^{*D-2}-1}{L^{*D}-1}\right)(1+\cos\theta_o) - 1 \qquad \text{(Equation 1)}$$

where θ_0 is the contact angle of a sessile droplet on a smooth functionalized solid surface. Figure 2C shows that the equilibrium contact angle increases with asperity length scale ratio L^*, for all values of fractal dimension D. For $L^* = 1$, the surface is smooth, and the contact angle is θ_0 (taken to be 120° in the plot) regardless of the fractal dimension. Increase in L^* corresponds to increase in the relative area fraction of air cavities which reduces surface wettability and leads to increase in equilibrium contact angle as per Equation 1. As $L^* \to \infty$, the solid area fraction of the topmost asperities in contact with the water droplet approaches zero, and the equilibrium contact angle asymptotically approaches the theoretical limit of 180°, the contact angle for water droplet in air. It is evident that for each D, there is a minimum L^* beyond which the equilibrium contact angle exceeds 150°, making the surface superhydrophobic; as D increases, superhydrophobicity is achieved for smaller values of L^*, equivalently, over a smaller range of asperity length scales. Figure 2C further shows that equilibrium contact angle increases with fractal dimension for a fixed L^* reflecting the enhanced nonwetting characteristic of rough surfaces.

Apart from contact angle *in situ*, θ, droplet mobility on a surface is additionally governed by contact angle hysteresis, θ_h, with superhydrophobic surfaces showing extremely small θ_h values. In dropwise condensation, θ_h values directly relate to the removal effectiveness of condensate droplets under the influence of external forces. Figure 2D presents the experimentally measured θ_h variation with contact

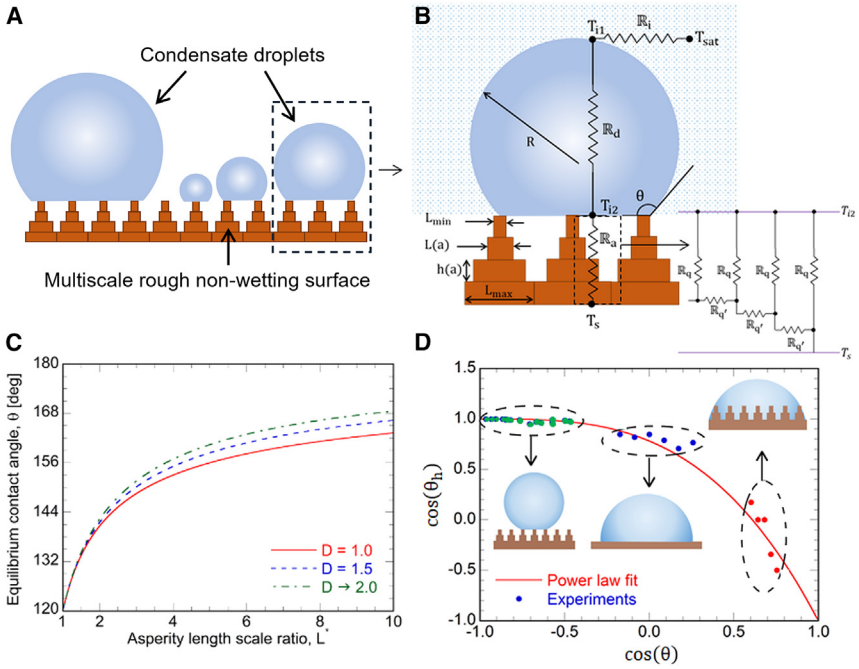

Figure 2. Thermal resistance network and surface wettability of a condensate droplet

(A) Schematic of condensation on a multiscale textured rough surface, (B) close-up view of heat transfer through a single droplet on a fractal surface representation, (C) variation of the equilibrium contact angle with asperity length scale ratio and fractal dimension, and (D) measurements of the contact angle hysteresis with equilibrium contact angle.

angle (θ) for a range of surfaces with different states of wettability. The data is categorized into three groups: measurements on (1) multiscale textured, unfunctionalized surfaces, (2) smooth unfunctionalized and functionalized surfaces, and (3) multiscale textured, functionalized surfaces. Multiscale textured, unfunctionalized surfaces exhibit Wenzel state of wettability with $\theta < 40^\circ$ and $\theta_h > 50^\circ$ (red markers). Smooth unfunctionalized and smooth functionalized surfaces demonstrate interim wettability between Wenzel and Cassie states, with θ in the range 80° to 120° and θ_h in the range 10° to 40° (blue markers). Multiscale textured, functionalized surfaces exhibit Cassie state of wettability characterized by larger contact angle values, $\theta > 130^\circ$ and smaller θ_h values in the range 1° to 10° (green markers). It is evident, therefore, that increasing θ corresponds to lower wetted area, leading to easy movement of droplet and smaller θ_h; conversely, a smaller contact angle results in droplet pinning or surface flooding, making it difficult for the droplet to move, thereby increasing θ_h. The variation of θ_h with θ may be represented by the following functional form, shown as the best-fit power law curve through the data points in Figure 2D:

$$\cos\theta_h = 1 - 2\left(\frac{1+\cos\theta}{2}\right)^3 \qquad \text{(Equation 2)}$$

where θ is given in terms of the fractal parameters of the surface by Equation 1. Note that Equation 2 obeys the physical consistency checks that when $\theta = 0^\circ$, the case of complete surface inundation, the droplets have no mobility, that is reflected in $\theta_h = 180^\circ$; on the other hand, when $\theta = 180^\circ$, the droplet has zero contact area with the surface leading to spontaneous droplet shedding or $\theta_h = 0^\circ$. Furthermore, by way of Equation 1, θ_h given by Equation 2 presents the first ever direct relationship between contact angle hysteresis and multiscale surface topography.

Droplet size distribution

Dropwise condensation is characterized by a spectrum of spherical condensate droplets of various size, R, on a multiscale rough nonwetting condensing surface, as shown in Figure 2A. At the smaller droplet sizes nucleation and growth are governed by direct accumulation of saturated vapor molecules onto the interface of condensate droplet and saturated air; after a critical droplet size, the growth is characterized by coalescence of condensate droplets. The resultant larger droplets by coalescence are either forced to move on the condensing surface under the effect of imbalanced gravitational force, leading to eventual shedding of condensate droplets (GDC), or they jump away from the condensing surface upon coalescence (JDC). The theoretical model is applicable to dropwise condensation, in general, unless distinguished by the superscript 'g' or 'j', for GDC or JDC, respectively. In GDC as well as JDC, the removal of condensate droplets leads to renewal of the condenser surface for fresh nucleation of smaller condensate droplets.

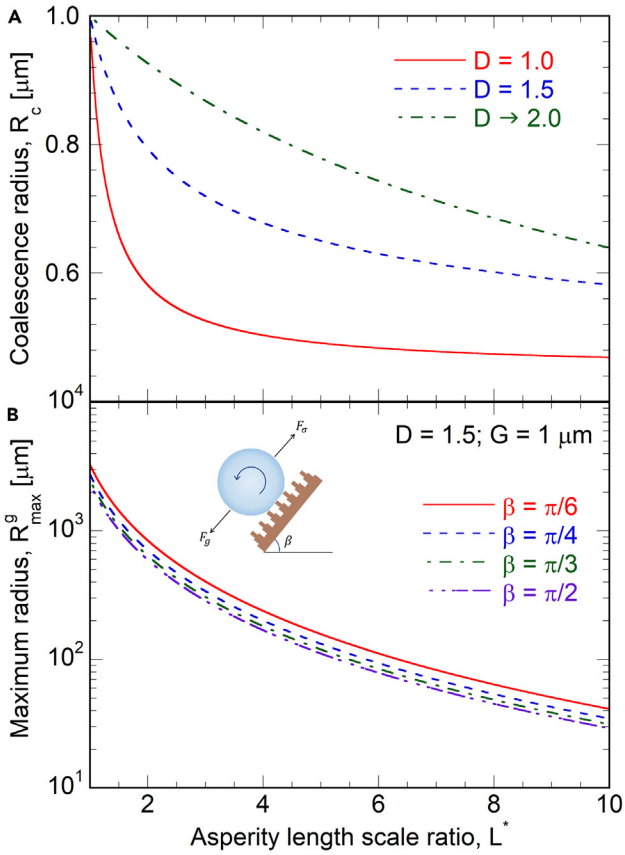

Figure 3. Coalescence radius and departure radius in terms of the fractal parameters

Variation with asperity length scale ratio, L^*, of (A) coalescence radius for a range of fractal dimension values and (B) maximum shedding radius in GDC mode of dropwise condensation for a range of surface inclination angles, for an illustrative $\Delta T = 10$ K.

The droplet size distribution may be obtained as follows. Condensation initiates with nucleation of droplets of radius, $R_{min} = \frac{2T_{sat}\sigma}{h_{fg}\rho\Delta T}$, in which σ is the condensate liquid-air interfacial tension, ρ is the density of water vapor, and h_{fg} is the latent heat of vaporization. As the droplets grow, they start to coalesce at a critical radius, $R_c = \frac{1}{4\sqrt{\mathbb{N}}}$,[6,32] that is dependent on the nucleation density of the droplets, $\mathbb{N}$, which scales with the surface area available for nucleation. Following the fractal model of a surface topography, the total asperity surface area when scaled with the projected base area is defined as the non-dimensional nucleation density of multiscale rough surfaces and is obtained as: $\frac{\mathbb{N}}{\mathbb{N}_o} = 1 + \frac{4D}{3-2D} G^{D-1} L_{max}^{1-D} (1 - L^{*2D-3})$ where $\mathbb{N}_o = 2.5\times10^{11}$ is the nucleation density on a smooth non-structured surface[32] for which $L^* = 1$. The expression for the total asperity surface area can be derived by considering the fractal characteristics of the surface wherein the height of each asperity element is related to its length scale and characteristic fractal parameters namely, D, G and L^*, as previously discussed by Jain and Pitchumani.[30] Therefore, the coalescence radius as a function of fractal parameters can be obtained as: $R_c = 0.25\left[\mathbb{N}_o\left(1+\frac{4D}{3-2D} G^{D-1} L_{max}^{1-D} (1 - L^{*2D-3})\right)\right]^{-0.5}$.

Nucleation density is a direct result of the driving potential for condensation of steam measured in terms of temperature difference ΔT. However, in the present study, the dependence of nucleation density N on temperature difference ΔT is not considered in accordance with existing theoretical models. However, it is intuitive that with increasing temperature difference ΔT, the nucleation density increases, leading to decreasing coalescence radius on the same available surface area (rough surface geometry) for condensation. Furthermore, significant increase in nucleation density and the corresponding reduction in coalescence radius will lead to penetration of condensate deep within the surface asperities resulting in a partial or fully Wenzel state of wettability, and a reduced condensation heat transfer performance. Such a dependence of condensation performance on temperature difference may be readily extended from the present analysis in a future study.

Figure 3A shows that the coalescence radius decreases with increase in asperity length scale ratio L^* for all values of fractal dimension D. Starting from $R_c = 1\ \mu m$ for $L^* = 1$ (smooth surface), as the asperity length scale ratio increases, the total area of solid asperities also increases, leading to greater nucleation density of condensate droplets, and a concomitant decrease in the coalescence radius. A similar trend holds for the scaling constant, G, where for fixed D and L^*, an increase in G leads to taller asperities spaced at a fixed distance with fixed roughness features leading to a larger area available for nucleation, thereby leading to lower coalescence radius, as evident from the equation for R_c. For

a fixed scaling constant and asperity length scale ratio, an increase in the fractal dimension D leads to a larger portion of (non-solid) air cavities which allows for more growth of condensate droplets before coalescence, hence the increasing coalescence radius as seen in Figure 3A.

For droplet departure in GDC on a surface inclined at an angle, β, measured counterclockwise from the horizontal (inset image in Figure 3B), at a certain droplet radius, $R = R^g_{max}$, the external force of gravity, $F_g = \frac{(2-3\cos\theta+\cos^3\theta)\pi\left(R^g_{max}\right)^3\rho g \sin\beta}{3}$, is balanced by the restoring capillary force, $F_\sigma = 2\sigma R^g_{max}\sin\theta(\cos(\theta-\theta_h)-\cos(\theta+\theta_h))$, which leads to a closed-form analytical expression for the maximum (departure) condensate droplet radius: $R^g_{max} = \left[\frac{6\sigma(\cos(\theta-\theta_h)-\cos(\theta+\theta_h))\sin\theta}{\pi\rho g(2-3\cos\theta+\cos^3\theta)\sin\beta}\right]^{1/2}$, where θ and θ_h are given by Equations 1 and 2, respectively. During surface condensation, condensate droplets periodically shed, renewing the surface for fresh nucleation. It is, therefore, desirable that condensate droplets shed at a smaller R^g_{max}, which would result in larger number of smaller droplets from fresh nucleation and higher frequency of shedding, overall leading to enhanced condensation heat transfer. Figure 3B shows that for a representative combination of fractal parameters (D = 1.5 and $G = 1\ \mu m$), R^g_{max} decreases by nearly two orders of magnitude with a 10-fold increase in asperity length scale ratio, L^*, for all values of condensing surface inclination, β. An increase in L^* increases the contact angle, θ (per Equation 1; Figure 2C), which leads to a decrease in θ_h (per Figure 2D), collectively leading to reduction in R^g_{max}. This trend points to the beneficial effect of multiscale surface texturing in reducing the departure radius and increasing the shedding frequency.

In the phenomenon of JDC, typically observed on nanostructured surfaces, the condensate droplets at coalescence radius (R_c) merge and spontaneously detach from the condensing surface.[27] Under these conditions, the maximum departing droplet radius can be obtained by the volume conservation as $R^j_{max} = 2^{\frac{1}{3}}\cdot R_c$. By considering the difference in maximum radius values of R^g_{max} and R^j_{max}, the theoretical model can be utilized for dropwise condensation on both hydrophobic and micro-nano scale superhydrophobic surface, in general.

Using the foregoing definitions of the minimum, coalescence, and maximum radii, we adopt the expressions for droplet size distribution from the literature.[6,32] For droplet size in the range, $R_{min} < R < R_c$, the condensate droplet growth is governed by the direct accumulation of vapor molecules on the liquid-air interface, whereas in the range of droplet size $R_c < R < R_{max}$, droplet growth is governed by coalescence of condensate droplets, where R_{max} refers to the maximum radius corresponding to the applicable condensation mode. The condensate droplet number density, $N(R)$, in units of $\#/m^3$, is thus given by

$$N(R) = \begin{cases} \frac{1}{3\pi R_c^3 R_{max}}\left(\frac{R_c}{R_{max}}\right)^{-2/3}\frac{R(R_c-R_{min})}{(R-R_{min})}\frac{A_2R+A_3}{A_2R_c+A_3}\exp(B_1+B_2) & R_{min}<R<R_c \\ \frac{1}{3\pi R^2 R_{max}}\left(\frac{R}{R_{max}}\right)^{-2/3} & R_c<R<R_{max} \end{cases} \quad \text{(Equation 3)}$$

in which,

$$B_1 = \frac{A_2}{\tau A_1}\left[\frac{R_c^2-R^2}{2} + R_{min}(R_c-R) - R_{min}^2\ln\left(\frac{R-R_{min}}{R_c-R_{min}}\right)\right];$$

$$B_2 = \frac{A_3}{\tau A_1}\left[R_c - R - R_{min}\ln\left(\frac{R-R_{min}}{R_c-R_{min}}\right)\right]; \tau = \frac{3R_c^2(A_2R_c+A_3)^2}{A_1\left(11A_2R_c^2-14A_2R_cR_{min}+8A_3R_c-11A_3R_{min}\right)};$$

$$A_1 = \frac{\Delta T}{h_{fg}\rho(1-\cos\theta)^2(2+\cos\theta)}; A_2 = \frac{\theta}{4k_w\sin\theta}; A_3 = \frac{1}{2h_i(1-\cos\theta)} + \pi R^2\mathbb{R}_a$$

It is noted that R_{min} is a function of the thermophysical parameters whereas R_c and R_{max} are governed additionally by L^*, D and G, which makes the droplet number density, $N(R)$, given by Equation 3, dependent on the fractal parameters of the multiscale rough condensing surface and the thermophysical parameters. The term $\mathbb{R}_a$ is defined in the following discussion.

Dropwise condensation heat transfer modeling

DWC heat transfer modeling is developed by first considering a single droplet heat transfer which is then integrated using droplet size distribution to obtain the overall heat transfer rate.

Single droplet heat transfer

Consider a condensate droplet of radius, R, and contact angle, θ, resting on a multiscale rough nonwetting surface, as shown in Figure 2B. The thermal resistance network between the saturated steam at temperature, T_{sat}, and the cold condensing surface at T_s is detailed in Figure 2B for a single droplet in the condensation process. Referring to Figures 2B and a single droplet heat transfer rate, $\dot{q}_d$, can then be calculated by considering the four thermal resistances and temperature drops from T_{sat} to T_s as follows:

(1) Temperature drop associated with the nucleation of condensate droplet can written as[32]: $\Delta T_c = \frac{R_{min}}{R}\Delta T$,

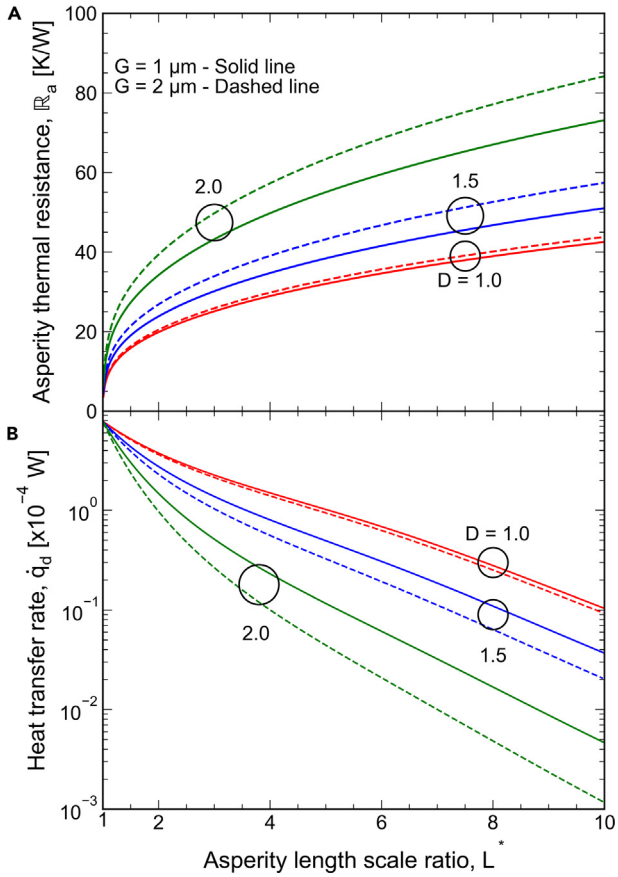

Figure 4. Thermal characteristics in terms of the fractal parameters

Variation of (A) asperity thermal resistance and (B) single condensate droplet heat transfer rate with asperity length scale ratio L^* for a range of G and D, for an illustrative $\Delta T = 10\ K$.

(2) Temperature drop during the direct accumulation of saturated vapor molecules onto the liquid-air interface is given by $\Delta T_i = T_{sat} - T_{i1} = \frac{\dot{q}_d}{h_i 2\pi R^2(1-\cos\theta)}$ where $h_i = \frac{2\alpha}{2-\alpha}\frac{1}{\sqrt{2\pi R_g T_s}}\frac{h_{fg}^2}{v_g T_s}$ is a thermodynamically determined interfacial heat transfer coefficient,[6,32] in which α is the ratio of number of vapor molecules that are captured by the liquid-air interface to the number of molecules approaching the interface in a steady state, R_g is the specific gas constant and v_g is the water vapor specific volume.

(3) Temperature drop associated with conduction within the droplet bulk, from the curved liquid-air interface (T_{i1}) to the flat interface of liquid and surface asperities (T_{i2}) is expressed as $\Delta T_d = T_{i1} - T_{i2} = \frac{\dot{q}_d \theta}{4\pi R k_w \sin\theta}$ where k_w is the thermal conductivity of water.[32]

(4) Temperature drop due to the layer of asperity network on the surface can be written as $\Delta T_a = T_{i2} - T_s = \dot{q}_d \mathbb{R}_a$ with asperity thermal resistance $\mathbb{R}_a$ given by the following equation

$$\mathbb{R}_a = \left(\frac{\xi}{1+\xi}\right)\left(\frac{D}{(2-D)A_t}\right)^{\frac{D}{2}}\left(\frac{G^{D-1}}{k_s L_{max}^D}\right)\left(\frac{1+\sqrt{1+4\xi}}{1+2\xi+\sqrt{1+4\xi}}\right) \quad \text{(Equation 4)}$$

where $\xi = \left[\frac{D(1-A_t)}{(2-D)A_t}\right]^{1/2}$, $A_t = \frac{D}{D-2}\left(\frac{L^{*2-D}-1}{L^{*2-D}-L^{*2}}\right)$ and k_s is the thermal conductivity of the solid material. Equation 4 considers a series and parallel network of conductive solid asperities and non-conductive infused material that yields the total equivalent asperity thermal resistance, $\mathbb{R}_a$, in terms of fractal parameters D, G and L^*.[31]

Figure 4A presents the variation of thermal resistance, $\mathbb{R}_a$, with asperity length scale ratio L^* for two scaling constant values, $G = 1\ \mu m$ and $2\ \mu m$, representative of chemically etched and electrodeposited SHS, respectively, and three fractal dimension values, $D = 1.0, 1.5$ and 2.0, covering the entire range of fractal topological dimension. Figure 4A shows that the asperity thermal resistance $\mathbb{R}_a$ increases with L^* for all combinations of G and D. For a given G and D, an increase in the asperity length scale ratio reduces the solid area fraction and increases the overall asperity height, both resulting in increased effective thermal resistance within the asperity layer. For the same reason, $\mathbb{R}_a$ also

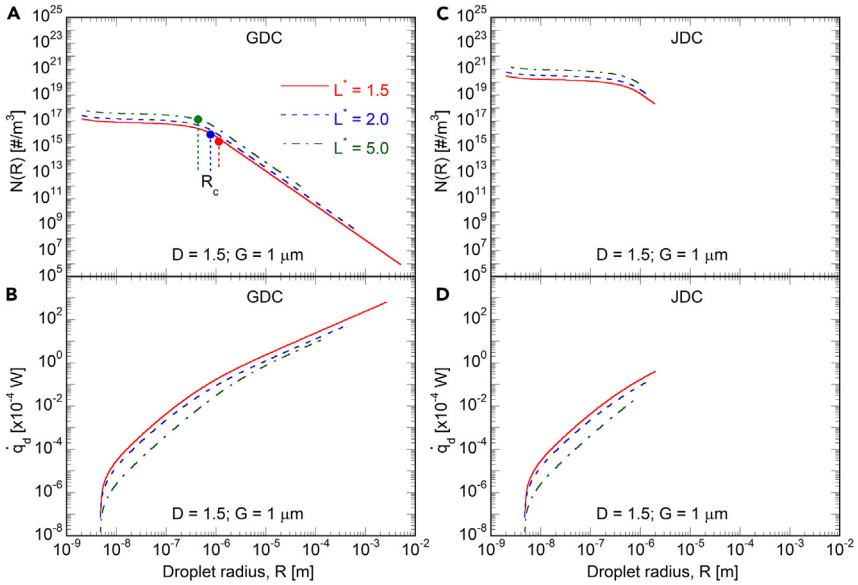

Figure 5. Condensate droplet statistics and heat transfer rate in terms of droplet size

Variation of (A) droplet density, $N(R)$, and (B) single droplet heat transfer rate, $\dot{q}_d$, for GDC mode of dropwise condensation and (C) droplet density, $N(R)$, and (D) single droplet heat transfer rate, $\dot{q}_d$ for JDC mode of dropwise condensation with droplet radius for a range of L^* values, for an illustrative $\Delta T = 10\ K$.

increases with increase in fractal dimension and/or scaling constant, as seen in Figure 4A. As physical consistency check, Figure 4A correctly shows that as asperity length scale ratio approaches unity, $L^* \rightarrow 1$, the multiscale rough surface approaches a conventional smooth surface, for which the asperity thermal resistance approaches zero for all values of D and G.

The total temperature difference between T_{sat} and T_s is the sum of the constituent four individual temperature drops, expressed as $\Delta T = \Delta T_c + \Delta T_i + \Delta T_d + \Delta T_a$. Substituting the expressions for each of the temperature differences from the foregoing discussion, we obtain a closed-form expression for heat transfer rate of a single condensate droplet of radius R as:

$$\dot{q}_d(R, \Delta T; D, G, L^*) = \frac{\pi R^2 \left(\Delta T - \frac{2T_{sat}\sigma}{Rh_{fg}\rho} \right)}{\frac{1}{2h_i(1 - \cos\theta)} + \frac{R\theta}{4k_w \sin\theta} + \pi R^2 \mathbb{R}_a} \qquad \text{(Equation 5)}$$

Equation 5 suggests that the heat transfer rate $\dot{q}_d$ varies with subcooling, ΔT, droplet size (R) and the fractal parameters, D, G, and L^* of the multiscale rough surface topography that govern both condensation surface wettability quantified in terms of the water contact angle (θ) and $\mathbb{R}_a$.

Figure 4B examines the characteristics of condensation heat transfer rate for a single droplet ($\dot{q}_d$) on a multiscale rough SHS, given by Equation 5, in terms of the variation of $\dot{q}_d$ with asperity length scale ratio L^*, for a range of D and G values. Figure 4B shows that for all combinations of D and G values, an increase in the asperity length scale ratio reduces the condensate droplet heat transfer rate, owing to the dominant increase in the asperity thermal resistance (evident from Equation 4; Figure 4A). Likewise, for a given asperity length scale ratio value, increase in D or G increases the asperity thermal resistance showing corresponding reduction in the heat transfer rate. Figure 4B also demonstrates the physical consistency check that as $L^* \rightarrow 1$, representing a smooth surface, the condensate droplet heat transfer rate approaches a maximum value corresponding to $\mathbb{R}_a = 0$ in Equation 5.

The overall dropwise condensation heat transfer on a multiscale surface is then obtained as an integral of the single droplet heat transfer rate ($\dot{q}_d$) discussed thus far weighted with the total number of droplets of a particular size, $N(R)$, as the kernel function. To this end, it is instructive to examine first the variation of $N(R)$ and $\dot{q}_d$ with the droplet radius for the different multiscale surface parameters, as presented in Figures 5A and 5B for GDC and Figures 5C and 5D for JDC, respectively. Microtextured surfaces undergoing GDC are best represented by a relatively higher value of scaling constant such as $G = 1\ \mu m$ as derived from the fast Fourier transform of surface profiles as described in Figure 1. For nanotextured surfaces exhibiting JDC, the scaling constant G value is obtained by conducting a fast Fourier transform of roughness profile obtained by image processing a typical nanotextured surfaces as provided by Miljkovic et al.[27] The resultant fractal parameters that best represent the nanotextured surface are: $D = 1.8$, $G = 0.1\ \mu m$ and $L^* = 10$. A physical consistency check on the derived fractal values is conducted by verifying that the fractal representation leads to about 1 μm total height of nanotextured asperities which closely matches the values obtained by Miljkovic et al.[27] Therefore, hereafter, representative scaling constant values of $G = 1\ \mu m$ for GDC and $G = 0.1\ \mu m$ for JDC are used in the theoretical model.

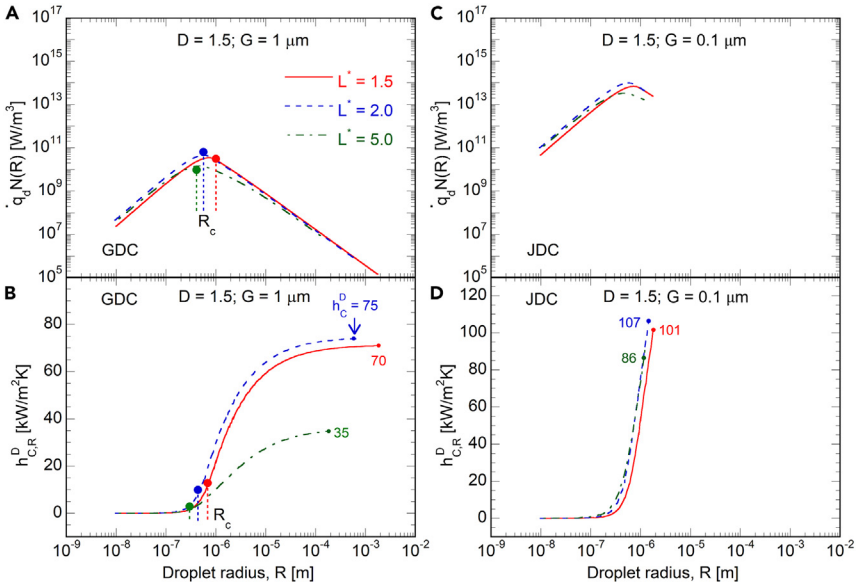

Figure 6. Contribution of droplet size to overall condensation heat transfer

Variation of (A) $\dot{q}_d \cdot N(R)$ and (B) $h^D_{C,R}$ for GDC and (C) $\dot{q}_d \cdot N(R)$ and (D) $h^D_{C,R}$ for JDC modes of dropwise condensation with droplet radius for a range of L^* values and for an illustrative $\Delta T = 10\ K$.

In Figure 5 the combination of $D = 1.5$ and $G = 1\ \mu m$ is used for GDC and $D = 1.5$ and $G = 0.1\ \mu m$ is used for JDC modes of dropwise condensation. The droplet size is seen to range between R_{min}, that is independent of L^*, and R^g_{max} or R^j_{max}, that is a function of the mode of condensate droplet removal and fractal parameters. It is evident from Figures 5A and 5C that for any value of asperity length scale ratio, the condensate droplet number density decreases with increase in droplet size, in two piecewise continuous regimes demarcated by the coalescence radius, R_c, as per Equation 3. During condensation, shedding of larger condensate droplets from the surface results in fresh nucleation of many smaller droplets. Therefore, for any condensing surface topology and condition, there are a larger number of smaller droplets, as seen from Figures 5A and 5C. For a given droplet size, a larger asperity length scale ratio results in higher condensate droplet density owing to the more frequent shedding of condensate droplets at a smaller departure radius (Figure 3B), leading to frequent fresh nucleation of smaller droplets. A direct comparison between Figures 5A and 5C reveals that the droplet number density for JDC is significantly higher than GDC owing to the early removal of droplets upon coalescence at smaller size in the case of JDC.

Figures 5B and 5D show the variation of single droplet heat transfer rate with droplet size, wherein the trendlines end at the respective largest droplet size values based on GDC and JDC modes of droplet removals, respectively. It is evident from Figures 5B and 5D that the heat transfer rate of a single condensate droplet increases with droplet size for a fixed asperity length scale ratio, for both GDC and JDC. For a given L^* (and D), the contact angle is constant (Equation 1), whereby increase in the droplet radius results in a larger contact area and a higher heat transfer rate. Similarly, with increase in L^*, through Figure 2C and Equation 1 it is evident that the contact angle increases. For a given droplet radius, R, the resulting reduction in the contact area with the condensing surface causes a reduction in the heat transfer rate, $\dot{q}_d$, as seen in Figures 5B and 5D. A further observation is that as $R \rightarrow R_{min}$, the corresponding single droplet heat transfer rate, $\dot{q}_d \rightarrow 0$, as per Equation 5.

It is evident from Figures 5A and 5B for GDC and Figures 5C and 5D for JDC, that $N(R)$ and $\dot{q}_d$ vary oppositely—droplet number density decreases whereas the heat transfer for a droplet increases—with increasing droplet size, that bears on the overall condensation heat transfer. Figures 6A and 6C examine the competing effects further by considering the contribution of all the droplets of each size, i.e., $\dot{q}_d \cdot N(R)$, to the overall condensation heat transfer, for a representative combination of $D = 1.5$ and $G = 1\ \mu m$ for GDC and $D = 1.5$ and $G = 0.1\ \mu m$ for JDC. A nonmonotonic variation of $\dot{q}_d \cdot N(R)$ is evident with the droplet radius, with droplets of the coalescence radius (R_c) corresponding to each L^* contributing to the maximum heat transfer rate. The increase in $\dot{q}_d \cdot N(R)$ for the smaller radius ($< R_c$) is due to the nearly constant number density (Figures 5A and 5C) with $\dot{q}_d$ increasing sharply (Figures 5B and 5D), whereas the decrease at the larger radius ($> R_c$) reflects the sharp decrease in the number density (Figures 5A and 5C). The competing effects leading to the non-monotonic trends of $\dot{q}_d \cdot N(R)$ are clearly visible for GDC (Figure 6A) owing to the larger droplet shedding sizes, whereas for JDC (Figure 6C) the portion of decreasing trend of $\dot{q}_d \cdot N(R)$ with R is shorter due to the maximum droplet size being much closer to the coalescence radius i.e., $R^j_{max} = 2^{\frac{1}{3}} \cdot R_c$. Further, nonlinearities and nonmonotonicity are evident in Figures 6A and 6C with respect to L^*: in the range of smaller droplet radius, $R < R_c$, $\dot{q}_d \cdot N(R)$ increases from $L^* = 1.5$ to 2.0 and decreases with further increase in the asperity aspect ratio from 2.0 to 5.0; however, for $R > R_c$, $\dot{q}_d \cdot N(R)$ monotonically decreases with increase in L^*.

Condensation heat transfer coefficient

The condensation heat transfer rate for a single droplet may be integrated with droplet size distribution to obtain the total condensation heat transfer rate, which when divided by the surface subcooling, ΔT, yields the condensation heat transfer coefficient. Considering the full droplet distribution spectrum from the minimum radius (R_{min}) to the maximum radius (R_{max}), the overall dropwise condensation heat transfer coefficient, h_C^D, is obtained as

$$h_C^D(\Delta T; D, G, L^*) = \int_{R_{min}}^{R_{max}} \frac{\dot{q}_d \cdot N(R)}{\Delta T} dR \quad \text{(Equation 6)}$$

where $\dot{q}_d$ (Equation 5) is a function of the droplet radius, R, and subcooling, ΔT, $N(R)$ is a piecewise continuous function given by Equation 3, and both $\dot{q}_d$ and $N(R)$ are dependent on the fractal parameters, D, G and L^*, of the multiscale rough surface. As a result, the condensation heat transfer coefficient is a function of subcooling and the multiscale rough surface topography. By choosing the appropriate values of maximum droplet size, the current model, as per Equation 6, yields the overall dropwise condensation heat transfer coefficient for GDC and JDC modes of condensation as $h_C^{D,g}(\Delta T; D, G, L^*) = \int_{R_{min}}^{R_{max}^g} \frac{\dot{q}_d \cdot N(R)}{\Delta T} dR$ and $h_C^{D,j}(\Delta T; D, G, L^*) = \int_{R_{min}}^{R_{max}^j} \frac{\dot{q}_d \cdot N(R)}{\Delta T} dR$, respectively.

The nonmonotonic variation of $\dot{q}_d \cdot N(R)$ with L^* (Figures 6A and 6C) combined with the fact that R_{max} decreases with increase in L^* for both GDC (Figure 3B) and JDC, suggests a complex relationship between the multiscale texture and the overall condensation heat transfer coefficient. It is instructive to unravel this relationship by examining the contribution of droplets of different size to overall heat transfer rate, by evaluating the integral in Equation 6 between R_{min} and R, i.e., $h_{C,R}^D = \int_{R_{min}}^{R} \frac{\dot{q}_d \cdot N(R)}{\Delta T} dR$, as R is gradually increased from R_{min} to R_{max}. Figures 6B and 6D show that for three different L^*, with $D = 1.5$ and $G = 1\ \mu m$ for GDC and with $D = 1.5$ and $G = 0.1\ \mu m$ for JDC, $h_{C,R}^D$ increases with R for all values of L^*. For gravity driven condensation (GDC), as evident from Figure 6B, the contributions of droplets of size less than about $0.1\ \mu m$ or greater than about $10\ \mu m$ on the condensation heat transfer coefficient are minimal, while droplets of radius in the range $0.1\ \mu m$ to $10\ \mu m$ have the most impact, as evidenced by the steep slope of $h_{C,R}^D$ variation with R.

From Figure 6A, we note that the range of $0.1\ \mu m < R < 10\ \mu m$ corresponds to $\dot{q}_d \cdot N(R) > \sim 10^9 \frac{W}{m^3}$. The maximum slope of the curves in Figure 6B occurs at the coalescence radius, R_c, as marked in Figure 6B, for each L^*, and correspond to the peak of the $\dot{q}_d \cdot N(R)$ variation in Figure 6A. For JDC, the steep behavior of $h_{C,R}^D$ variation with R is similar to that of GDC, however it occurs at lower values of droplet radius R. For JDC, the significantly higher values of droplet number density even for lower values of droplet size R when multiplied with the increasing trend of $\dot{q}_d$ with R leads to sharp increase in $h_{C,R}^D$ values as seen from Figure 6D. Even though there is similarity of steep behavior of $h_{C,R}^D$ with R at about respective coalescence radius values, the comparison between GDC (Figure 6B) and JDC (Figure 6D) shows that JDC offers more contribution of smaller droplet toward overall condensation than GDC, owing to the extremely early removal of droplets in JDC mode.

Note that $h_{C,R}^D$ evaluates to the overall condensation heat transfer coefficient, h_C^D (Equation 6), for $R = R_{max}$, as shown by the ending values of each curve in Figures 6B and 6D. Figures 6B and 6D further elucidate the competing effects of multiscale surface topography, discussed in Figures 6A and 6C, on the overall dropwise condensation heat transfer. An increase in L^* from 1.5 to 2.0 results in increasing h_C^D from 70 kW/m^{2}K to 75 kW/m^{2}K for GDC and from 101 kW/m^{2}K to 107 kW/m^{2}K for JDC; with further increase in L^* from 2.0 to 5.0, however, h_C^D decreases to 35 kW/m^{2}K and 86 kW/m^{2}K for GDC and JDC modes of condensation, respectively. The enhancement in dropwise condensation heat transfer coefficient with multiscale texturing is evident for all three L^* values, in comparison to the heat transfer coefficient of $h_C^F \approx 10$ kW/m^{2}K for film-wise condensation at $\Delta T = 10\,^\circ$C. However, the nonmonotonic variation of h_C^D with L^* clearly points to an optimal multiscale nonwetting surface topography that maximizes condensation heat transfer.

Figures 7A and 7B examine the variation of overall condensation heat transfer coefficient for GDC, $h_C^{D,g}$, and for JDC, $h_C^{D,j}$, respectively, with asperity length scale ratio L^* for a range of fractal dimension values and for a fixed value of $G = 1\ \mu$m. As $L^* \to 1$, h_C^D approaches that of smooth functionalized hydrophobic surface. As L^* increases from unity, the increase in the droplet number density compared to an insignificant reduction in single droplet heat transfer rate along with increase in droplet departure frequency at a smaller R_{max}, collectively results in enhanced overall condensation heat transfer performance for both GDC and JDC modes of dropwise condensation. For GDC, Figure 7A reveals that the overall condensation heat transfer coefficient is maximized for $L^* \approx 2.2$ for $D \to 2.0$, beyond which, reduction in single droplet heat transfer rate dominates the modest increase in droplet number density, collectively reducing $h_C^{D,g}$. For extremely high asperity length scale ratio, as $L^* \to \infty$, it is seen in Figure 7A that $h_C^{D,g} \to 0$ for all D. As $L^* \to \infty$, the contact angle, as per Equation 1, approaches 180°, which theoretically signifies no contact of condensate droplets with the surface, that is reflected in the condensation heat transfer coefficient asymptotically approaching zero.

The trend of overall condensation heat transfer coefficient $h_C^{D,j}$ with asperity length scale ratio, for three representative values of fractal dimensions for jumping droplet mode of condensation is similar to that of GDC. Figure 7B shows that the maximum JDC performance occurs for $L^* \approx 2.2$ and $D \to 2.0$. On the other extreme, as $L^* \to \infty$ the $h_C^{D,j}$ curves are seen to decrease asymptotically to zero, owing to the contact angle values of condensate droplets approaching to 180°, similar to that of GDC. However, due to extremely low sizes of departing droplets in JDC modes of condensation, for the same values of asperity length scale ratio and fractal dimension, Figure 7B shows much higher performance for JDC compared to that of GDC from Figure 7A. In addition, the rate of decrease of heat transfer coefficient with asperity length scale ratio for all values of D is much lower for JDC than GDC. In gravity driven condensation, the decreasing trend of $h_C^{D,g}$ with L^* results from the dual effect of increasing contact angle and reduced conduction within the asperities collectively reducing the single droplet heat transfer rate. For JDC, the absence of larger sized droplets leads to a similar effect of reduced single droplet heat transfer rate but to a lower extent compared to GDC.

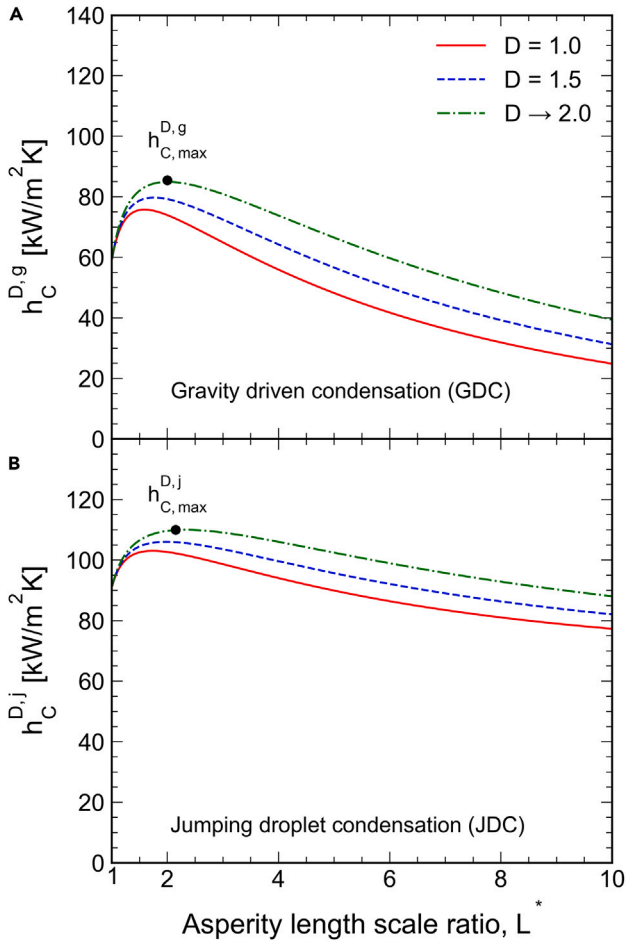

Figure 7. Optimum fractal parameter values for maximum condensation heat transfer

Variation of dropwise condensation heat transfer coefficient for (A) GDC and (B) JDC modes with asperity length scale ratio for different fractal dimension, D, for an illustrative $\Delta T = 10\ K$.

Figures 7A and 7B present the theoretical maximum dropwise condensation heat transfer values corresponding to a perfect Cassie state of wettability as defined by Equation 1 for GDC and JDC modes of condensation, respectively. The absolute maximums in Figures 7A and 7B are marked with notations $h_{C,max}^{D,g}$ and $h_{C,max}^{D,j}$. In actual steam condenser conditions under vacuum, though, condensate droplet dynamics is far from ideal and can suffer from possible Cassie to Wenzel transition. For instance, with increasing surface subcooling, condensate droplets start nucleating deep within the asperity valleys leading to a degraded wettability state than the ideal Cassie state defined by Equation 1. Such a behavior is observed to be characteristically valid for both GDC and JDC modes of dropwise condensation. The resulting higher pinning of condensate droplet to surface degrades condensation heat transfer and the theoretical maximum given by the model, $h_{C,max}^{D,g}$ and $h_{C,max}^{D,j}$, constitutes *upper bounds* of condensation heat transfer for the respective modes of condensation, GDC and JDC. On the other hand, the fully film-wise condensation heat transfer coefficient, h_C^F, given by the classical Nusselt correlation[33] represents the *lower bound* of condensation heat transfer:

$$h_C^F = 0.729\left[\frac{g\rho_l(\rho_l - \rho_v)k_l^3 h_{fg}}{\mu_l D_0 \Delta T}\right] \quad \text{(Equation 7)}$$

where g, ρ_l, ρ_v, k_l, h_{fg} and μ_l represent the acceleration due to gravity, liquid density, vapor density, thermal conductivity, latent heat of vaporization, and dynamic viscosity of water.

Experimental studies

With the bounds of condensation heat transfer coefficient defined by $h_{C,max}^{D,g}$ (or $h_{C,max}^{D,j}$) and h_C^F, we examine the experimental measurements of steam condensation heat transfer coefficient on two categories of surfaces. In the first, multiscale rough superhydrophobic surfaces were

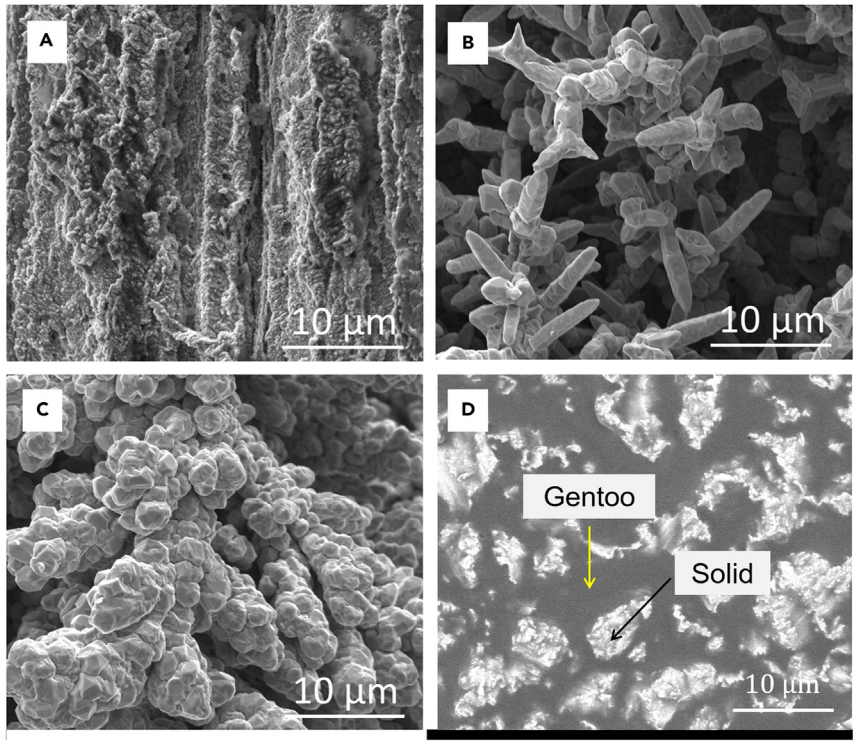

Figure 8. Morphology of various nonwetting surfaces

Scanning electron microscope images of (A) chemically etched SHS, (B) 0.7 *V* electrodeposited SHS, (C) 1.1 *V* electrodeposited SHS and (D) chemically etched Gentoo SIS. Scale bar size is 10 µm.

fabricated using the methods of chemical etching and electrodeposition at two overpotential values of 0.7 *V* and 1.1 *V* as described in the STAR Methods section. Figures 8A–8C show scanning electron microscope images elucidating the microstructural details of chemically etched, 0.7 *V* electrodeposited, and 1.1 *V* electrodeposited surfaces, respectively. The progressively aggressive multiscale texturing of the surfaces from etching to the low voltage electrodeposition and then the high voltage electrodeposition is evident from Figures 8A–8C, and point to the ability to tailor the texturing through appropriate selection of the fabrication method and parameters. The extent of multiscale texturing on each of the surfaces is further seen from the fractal parameters, D, G, and L^*, calculated on the surfaces from their respective power spectra, and summarized in Table 1. The fractal dimension values range from 1.6 to 1.9, G increases from 1 μm to 2 μm, and L^* ranges from 5 to 8, confirming the increasingly multiscale fractal structures in Figures 8A–8C.

The textured surfaces were rendered superhydrophobic by functionalization with stearic acid, margaric acid or mercaptan, applied as discussed in the STAR Methods section. The wetting characteristics of the different surface designs, resulting from a combination of texturing and functionalization that formed conformal coatings on the surfaces, are seen in the measured equilibrium contact angle values presented in Table 1. All surfaces, regardless of texturing method or functionalization agent showed contact angle values well above 150°, that confirms their superhydrophobicity. There is no significant variation in the contact angle among the different conformal functionalization coatings. The contact angle values are seen to increase with the fractal parameters, with the 1.1 *V* electrodeposited surface exhibiting contact angle greater than 160°. Table 1 further shows parenthetically the contact angle values predicted by the theoretical wettability model, Equation 1, based on the fractal parameters. The excellent agreement between the measured and predicted angles on the different surfaces confirms the validity of the model.

In addition to multiscale textured SHS, a recent class of surfaces called solid-infused surfaces (SIS) was also fabricated as described in the method details section. The SIS incorporates a nonwetting commercial thermosetting polymer, Gentoo, in the asperity interstices to form a hybrid metal/polymer surface, as seen in the SEM image of the surface in Figure 8D and from the smaller values of its fractal parameters, $D = 1.1$, $G = 0.2\ \mu m$, and $L^* = 2$. The solid infusion in the asperity valleys avoids the Cassie-to-Wenzel state transition that degrades the wettability of SHS. In this sense, SIS is similar to lubricant-infused surfaces (LIS), but unlike LIS that inevitably suffers lubricant drainage and transitions to SHS, SIS does not undergo any material loss or degradation of its wettability characteristic and remains robust over prolonged use, as shown in previous studies.[19,20] For etched, 0.7 *V* electrodeposited and 1.1 *V* electrodeposited SIS, contact angle values were measured to be 128°, 132°, and 127° and the contact angle hysteresis values were 13°, 12°, and 13°.

Figure 9 shows the variation of the measured condensation heat transfer coefficient with surface subcooling for the SHS with the three different textures and the three different functionalization agents and the SIS with the three different textures studied. Figure 9 also shows

Table 1. Fractal and wetting parameters of the various nonwetting surfaces studied

				Equilibrium contact angle, θ (Predicted) [°]		
Surface	D	G (μm)	L^*	Mercaptan	Margaric acid	Stearic acid
Etched SHS	1.6	1.0	5	154 (152)	155 (154)	156 (156)
Electrodeposited SHS, 0.7 *V*	1.7	1.2	6	159 (157)	158 (156)	160 (157)
Electrodeposited SHS, 1.1 *V*	1.9	2.0	8	161 (162)	160 (161)	162 (163)

heat transfer coefficient, h_C^F, for FWC obtained from the Nusselt equation (Equation 7), which constitutes a *lower bound* for condensation heat transfer. Following the trend of decreasing h_C^F with increasing subcooling, ΔT, in the classical Nusselt equation, Figures 9A–9C show that the heat transfer coefficient for the SHS and the SIS also decrease with increasing subcooling, regardless of texturing or functionalization (in the case of SHS). With increase in surface subcooling, the condensate vapor (steam) penetrates deeper within the asperities and nucleation and condensate droplet growth leads to higher pinning of droplets onto condenser surfaces, leading to decrease in heat transfer performance.

Figure 9A shows that for lower surface subcooling values, the etched SHS show dropwise condensation with higher condensation heat transfer coefficient values compared to film-wise condensation. However, at the higher surface subcooling values ($\Delta T \approx 17.5$ K), a diminishing improvement is seen due to the pinning of condensate droplets to the surface. Among the three functionalization coatings, stearic acid functionalization is seen to yield higher heat transfer coefficient compared to margaric acid and mercaptan, both of which lead to nearly the same heat transfer coefficient. Similarly, for the electrodeposited SHS, as seen from Figures 9B and 9C, the relatively deeper asperities in the textures, as evident from higher D, G and L^* values in Table 1, promote pinning of the condensate droplets, leading to lower heat transfer coefficient values compared to the etched SHS. Hence, for all functionalizing agents, the electrodeposited SHS show a marginal improvement when compared to film-wise condensation *lower bound*, with the difference further diminishing at the higher surface subcooling values.

In SIS, the cured polymer present in the interstitial asperity space eliminates the penetration of condensate droplets deep into the asperity valleys that reduced the performance of SHS. As a result, vigorous dropwise condensation is preserved leading to significantly higher heat transfer coefficient compared to SHS and well above the film-wise condensation heat transfer lower bound, as evident from Figures 9A–9C. The heat transfer coefficient for condensation on SIS is about three-to 4-fold that on SHS and film-wise condensation, at all subcooling values.

In Figure 10, the experimentally obtained condensation heat transfer coefficients are compared against the lower bound, $h_C^F(\Delta T)$, for FWC and the absolute theoretical maximum for JDC mode, $h_{C,max}^{D,j}$, in terms of a non-dimensional heat transfer coefficient defined as $\frac{h_C - h_C^F}{h_{C,max}^{D,j} - h_C^F}$. For perfect jumping droplet mode of DWC, $\frac{h_C - h_C^F}{h_{C,max}^{D,j} - h_C^F}$ takes the value of 1, whereas for FWC, $\frac{h_C - h_C^F}{h_{C,max}^{D,j} - h_C^F}$ takes the value of 0, as shown by the upper (red solid line) and lower (blue solid line) bounds in Figure 10. The second intermediate reference value arises from the absolute maximum performance in gravity driven condensation (GDC) mode, wherein the non-dimensional heat transfer coefficient is equal to 0.74 for $h_C = h_{C,max}^{D,g}$ i.e., $\frac{h_{C,max}^{D,g} - h_C^F}{h_{C,max}^{D,j} - h_C^F} = 0.74$. Using the non-dimensional measure of heat transfer coefficient $\frac{h_C - h_C^F}{h_{C,max}^{D,j} - h_C^F}$, and from Figure 10, it is evident that theoretical maximum gravity driven DWC performance is about 74% of the theoretical maximum JDC performance over FWC.

The experimental data in Figure 10 can be grouped into various categories. First, it includes the measurements taken in the present study spanning the three different fabrication methods and surface treatments all leading to micro scale texturing and exhibited gravity assisted dropwise condensation, shown by the open, purple-colored markers in Figure 10. Second, a set of data compiled from several literature studies, further categorized into two groups: first, gravity assisted dropwise condensation (GDC) on microtextured superhydrophobic surfaces[7–9] shown by the filled purple-colored markers and secondly, condensation on nanotextured surfaces[27] under two different modes of JDC (open blue circular markers) and GDC (open blue diamond markers) in Figure 10.

Figure 10 shows that microtextured SHS surfaces undergoing gravity driven condensation from the present work and from various literature studies[7–9] (purple colored markers) improves over FWC with $\frac{h_C - h_C^F}{h_{C,max}^{D,j} - h_C^F}$ values ranging up to ~0.3 at the lower surface subcooling and up to ~0.1 for the higher surface subcooling. It is evident that all the microtextured SHS data presented, regardless of source, fall in a band indicated by the bottommost shaded region in Figure 10, and are considerably below the theoretical upper bounds of JDC and GDC, with $\frac{h_C - h_C^F}{h_{C,max}^{D,j} - h_C^F} = 1$ (solid red line), and 0.74 (dashed brown line), respectively. The gaps to the upper bounds, shaded in yellow and further the light-red-shaded region in the plot, represent the possible opportunity for enhancement to the full potential of GDC and JDC, respectively, through suitable surface design and tailoring.

Figure 10 also presents the measured heat transfer coefficient on SIS fabricated in this study, in terms of the dimensionless $\frac{h_C - h_C^F}{h_{C,max}^{D,j} - h_C^F}$, shown by the filled green markers in the plot. The condensation heat transfer on SIS is seen to lie in the yellow-shaded area, with $\frac{h_C - h_C^F}{h_{C,max}^{D,j} - h_C^F}$ ranging from ~0.4 to ~0.6 at the smaller subcooling and from about 0.15 to ~0.25 at the larger values of surface subcooling, overall indicating a significant improvement over microtextured SHS for all subcooling.

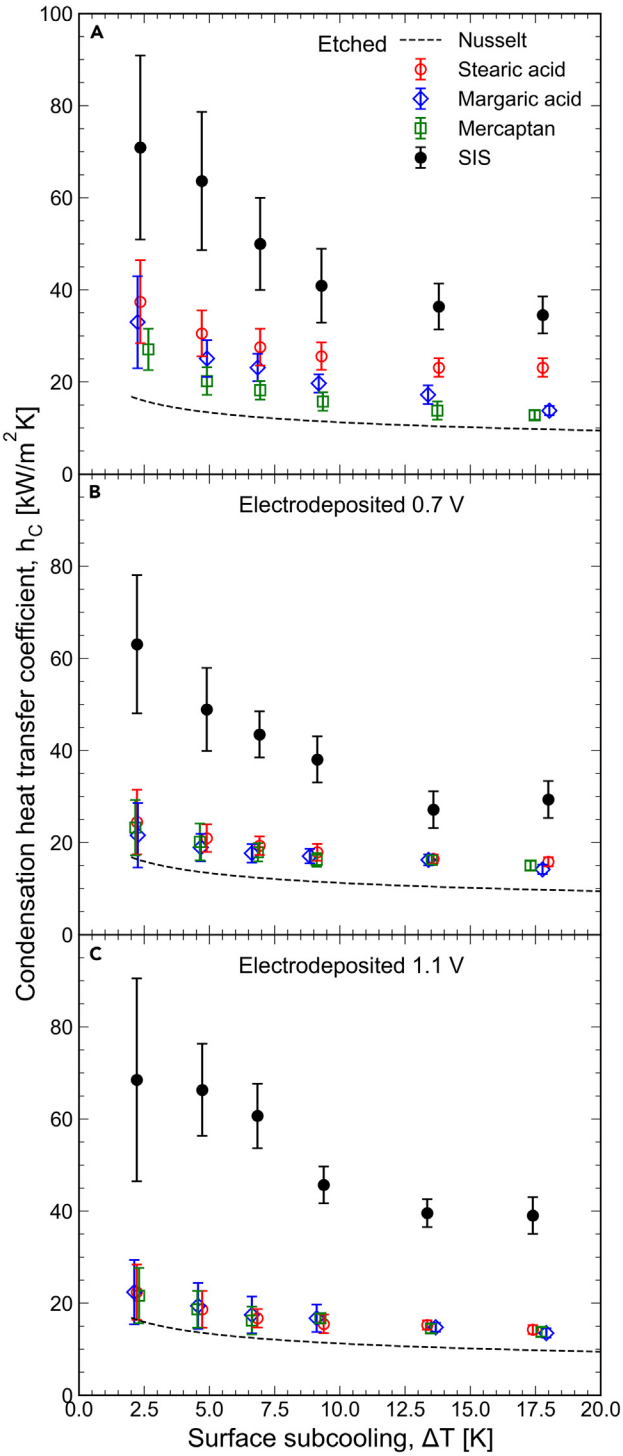

Figure 9. Experimentally measured condensation heat transfer coefficient on different surfaces

Variation of the measured condensation heat transfer coefficient with surface subcooling for (A) etched, (B) 0.7 *V* electrodeposited, and (C) 1.1 *V* electrodeposited SHS and SIS. Data are represented as mean ± SD.

In addition to gravity assisted condensation data on microtextured SHS and SIS surfaces, Figure 10 further includes the literature data on nanotextured surfaces undergoing JDC (blue open circular markers) that show significant improvement over GDC on microtextured surfaces and FWC. However, the superior performance is restricted to condensation conditions of lower supersaturation, as reported by Miljkovic

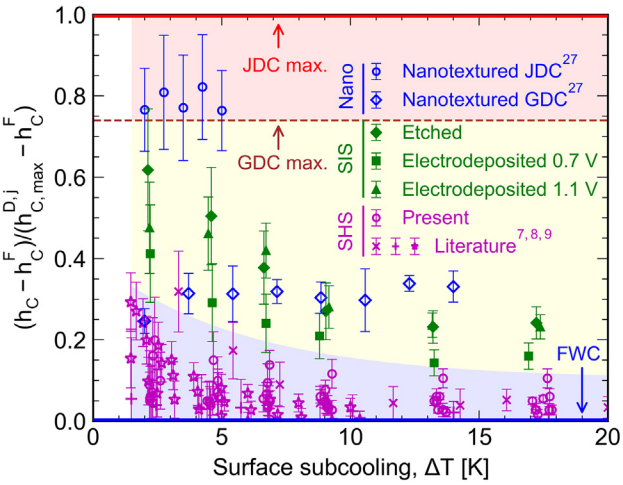

Figure 10. Experimental data relative to the lower and upper bounds on the condensation heat transfer coefficient

Variation of a non-dimensional heat transfer coefficient $\left(\frac{h_C - h_C^F}{h_{C,max}^{D,j} - h_C^F}\right)$ with surface subcooling ΔT for SHS in the present and literature studies in comparison to SIS introduced in this study. Data are represented as mean ± 95% CI (present and SIS) and mean ± SD (all referenced literature data).

et al.[27] At higher supersaturation levels, denoted by open blue-colored diamond markers in Figure 10, the performance degrades to the lower values of about $\frac{h_C - h_C^F}{h_{C,max}^{D,j} - h_C^F} = 0.3$, that are on par with SIS. Moreover, considering that the nanostructures are prone to mechanical failures under prolonged or adverse condensation conditions, the sustained superior dropwise condensation on solid-infused surfaces (SIS) is noteworthy.

Conclusions

In this article, we presented the first ever theoretical model for dropwise condensation heat transfer on multiscale rough dry nonwetting surface, characterized uniquely in terms of the surface fractal parameters. The fractal surface parameters were used to determine the building blocks of contact angle, contact angle hysteresis, and droplet size distribution, droplet departure size for two modes of condensation (GDC and JDC) and, cumulatively, the condensation heat transfer coefficient. Through systematic analysis, several fundamental insights were derived.

(1) it was shown quantitatively that the initial condensate droplet growth through direct vapor accumulation contributes insignificantly toward the overall condensation heat transfer, whereas it is the coalescence dominated growth that accounts for most of the condensation heat transfer performance in gravity driven dropwise condensation.
(2) for a given combination of fractal dimension, D, scaling constant, G, and surface subcooling, ΔT, there exists an optimum asperity length scale ratio $1.5 < L^* < 3.0$ that maximizes condensation heat transfer coefficient by trading off between non-wettability and the asperity thermal resistance leading to optimal surface texture designs for both GDC and JDC modes.
(3) by considering a perfect Cassie state of wettability, the model yields theoretical *upper* bounds for GDC and JDC heat transfer coefficient values as a function of surface fractal parameters (D, G and L^*) and surface subcooling (ΔT).
(4) by pooling experimental measurements of condensation heat transfer coefficient on multiscale rough dry nonwetting surfaces it is seen that microtextured SHS improves upon the *lower* bound given by the classical Nusselt theory but leaves much room for enhancement with respect to the theoretical *upper* bound. SIS, on the other hand, offers one surface engineering example that strives to bridge the gap to the upper bound.
(5) the much-touted JDC observed on nanotextured surfaces shows superior performance only in the limited operating conditions of lower supersaturation, whereas at higher supersaturation the performance degrades. Considering the durability and scalability limitations of nanotextured surfaces and their performance degradation at higher supersaturation, SIS provides a viable, robust option for sustained superior dropwise condensation.
(6) the model presented in the study can be used to predict the *upper bound* of condensation heat transfer coefficient for a given surface and condensation conditions or, alternatively, to design optimum surface topography for *maximum* condensation heat transfer performance.

The main contribution of the article is the development of the limits of condensation heat transfer for a dry nonwetting surface with a given texture. With growing number of studies that tout higher and higher heat transfer coefficients on nonwetting surfaces, it begs the question as to how high of a heat transfer coefficient can be theoretically possible for a given surface, and the present study

provides a valuable fundamental treatise in this regard. The article assembled data presented in the literature so far on a common plot (Figure 10) and it is encouraged that future studies report their data in the format of Figure 10 to assess their performance against the theoretical limits.

Limitations of the study

Although the study focused on a broad class of *dry* nonwetting surfaces, the theoretical foundation presented herein may be readily extended to lubricant infused surfaces in a future work. The contribution of temperature difference ΔT between the cold surface and saturated steam toward the nucleation density and the wettability of condensate droplets, leading to effects on the overall condensation performance is an area for further work building on the present article. In addition, detailed experimental analysis of the coalescence induced growth of droplets inside the multiscale asperity structures are needed to better understand the dynamic wettability and its effects on overall condensation heat transfer performance. Moreover, the effects of nucleation of condensate droplets deep within the asperities and their growth dynamics thereafter will be considered theoretically in a future work. Other special situations such as those discussed in refs. Kim and Kim[34] and Kim and Kim[35] may also be incorporated in future extensions of the work presented here.

RESOURCE AVAILABILITY

Lead contact

Further information requests should be directed to the lead contact, R.P. (pitchu@vt.edu).

Materials availability

Materials used in the study are commercially available as listed in the key resources table.

Data and code availability

- All data are reported in the article, the STAR Methods, or the supplemental information file.
- The study does not report any original code.
- Any additional information may be requested from the lead contact.

ACKNOWLEDGMENTS

The authors acknowledge Dr. Ryan Stoddard for his assistance with the experimental studies. The material reported in this publication is based upon work supported by the U.S. Department of Energy under Award Number DE-FE0031556. This work used shared facilities at the Nanoscale Characterization and Fabrication Laboratory, which is funded and managed by Virginia Tech's Institute for Critical Technology and Applied Science. Additional support is provided by the Virginia Tech National Center for Earth and Environmental Nanotechnology Infrastructure (NanoEarth), a member of the National Nanotechnology Coordinated Infrastructure (NNCI), supported by the U.S. National Science Foundation through Award Numbers ECCS 1542100 and ECCS 2025151. The views and opinions of authors expressed herein do not necessarily state or reflect those of the United States Government or any agency thereof.

AUTHOR CONTRIBUTIONS

S.H. and R.P. designed the study; S.H. conducted the experiments; S.H. and R.P. analyzed the data, wrote and edited the paper; R.P. was the principal investigator and supervised the work.

DECLARATION OF INTERESTS

R.P. has a patent application related to this work, which is cited as ref. 21.

STAR★METHODS

Detailed methods are provided in the online version of this paper and include the following:

- KEY RESOURCES TABLE
- METHOD DETAILS
  - Surface fabrication, characterization, and functionalization
  - Experimental methodology
- QUANTIFICATION AND STATISTICAL ANALYSIS

SUPPLEMENTAL INFORMATION

Supplemental information can be found online at https://doi.org/10.1016/j.isci.2024.111059.

Received: September 26, 2023
Revised: July 28, 2024
Accepted: September 24, 2024
Published: September 27, 2024

REFERENCES

1. Solomon, B.R., Khalil, K.S., and Varanasi, K.K. (2014). Drag Reduction Using Lubricant-impregnated Surfaces in Viscous Laminar Flow. Langmuir *30*, 10970–10976. https://doi.org/10.1021/la5021143.
2. Hatte, S., and Pitchumani, R. (2021). Analytical Model for Drag Reduction on Liquid-infused Structured Non-wetting Surfaces. Soft Matter *17*, 1388–1403. https://doi.org/10.1039/D0SM01272F.
3. Tuo, Y., Zhang, H., Rong, W., Jiang, S., Chen, W., and Liu, X. (2019). Drag Reduction of Anisotropic Superhydrophobic Surfaces Prepared by Laser Etching. Langmuir *35*, 11016–11022. https://doi.org/10.1021/acs.langmuir.9b01040.
4. Hatte, S., and Pitchumani, R. (2020). Fractal Model for Drag Reduction on Multiscale Nonwetting Rough Surfaces. Langmuir *36*, 14386–14402. https://doi.org/10.1021/acs.langmuir.0c02790.
5. Kant, K., and Pitchumani, R. (2021). Laminar drag reduction in microchannels with liquid infused textured surfaces. Chem. Eng. Sci. *230*, 116196. https://doi.org/10.1016/j.ces.2020.116196.
6. Stoddard, R., Nithyanandam, K., and Pitchumani, R. (2021). Steam Condensation Heat Transfer on Lubricant-infused Surfaces. iScience *24*, 102336. https://doi.org/10.1016/j.isci.2021.102336.
7. Zhang, T.Y., Mou, L.W., Zhang, J.Y., Fan, L.W., and Li, J.Q. (2020). A visualized study of enhanced steam condensation heat transfer on a honeycomb-like microporous superhydrophobic surface in the presence of a non-condensable gas. Intern. J. Heat Mass Trans. *150*, 119352. https://doi.org/10.1016/j.ijheatmasstransfer.2020.119352\.
8. Wen, R., Xu, S., Zhao, D., Yang, L., Ma, X., Liu, W., Lee, Y.C., and Yang, R. (2018). Sustaining enhanced condensation on hierarchical mesh-covered surfaces. Natl. Sci. Rev. *5*, 878–887. https://doi.org/10.1093/nsr/nwy098.
9. Wang, R., Wu, F., Xing, D., Yu, F., and Gao, X. (2020). Density maximization of one-step electrodeposited copper nanocones and dropwise condensation heat-transfer performance evaluation. ACS Appl. Mater. Interfaces *12*, 24512–24520. https://doi.org/10.1021/acsami.0c05224.
10. Allred, T.P., Weibel, J.A., and Garimella, S.V. (2018). Enabling highly effective boiling from superhydrophobic surfaces. Phys. Rev. Lett. *120*, 174501. https://doi.org/10.1103/PhysRevLett.120.174501.
11. Fuller, A.M., and Pitchumani, R. (2023). Long Term Durability of a Lubricant-Infused Surface for Dew Harvesting. Langmuir *39*, 9885–9892. https://doi.org/10.1021/acs.langmuir.3c01123.
12. Maynes, D., Webb, B.W., and Davies, J. (2008). Thermal Transport in a Microchannel Exhibiting Ultrahydrophobic Microribs Maintained at Constant Temperature. J. Heat Transfer *130*, 1–8. https://doi.org/10.1115/1.2789715.
13. Hatte, S., and Pitchumani, R. (2021). Analysis of Laminar Convective Heat Transfer Over Structured Non-Wetting Surfaces. Int. J. Heat Mass Transf. *167*, 120810. https://doi.org/10.1016/j.ijheatmasstransfer.2020.120810.
14. Hatte, S., and Pitchumani, R. (2021). Analysis of Convection Heat Transfer on Multiscale Rough Superhydrophobic and Liquid Infused Surfaces. Chem. Eng. J. *424*, 130256. https://doi.org/10.1016/j.cej.2021.130256.
15. Fuller, A., Kant, K., and Pitchumani, R. (2024). Analysis of Freezing of a Sessile Water Droplet on Surfaces over a Range of Wettability. J. Colloid Interface Sci. *653*, 960–970. https://doi.org/10.1016/j.jcis.2023.09.119.
16. Ruan, M., Li, W., Wang, B., Deng, B., Ma, F., and Yu, Z. (2013). Preparation and Anti-icing Behavior of Superhydrophobic Surfaces on Aluminum Alloy Substrates. Langmuir *29*, 8482–8491. https://doi.org/10.1021/la400979d.
17. Hatte, S., Kant, K., and Pitchumani, R. (2023). Freezing Characteristics of a Water Droplet on a Multiscale Superhydrophobic Surface. Langmuir *39*, 11898–11909. https://doi.org/10.1021/acs.langmuir.3c01705.
18. Hatte, S., Stoddard, R., and Pitchumani, R. (2022). Generalized Analysis of Dynamic Flow Fouling on Heat Transfer Surfaces. Intern. J. Heat Mass Trans. *188*, 122573. https://doi.org/10.1016/j.ijheatmasstransfer.2022.122573.
19. Hatte, S., and Pitchumani, R. (2022). Analysis of Silica Fouling on Nonwetting Surfaces. Soft Matter *18*, 3403–3411. https://doi.org/10.1039/D2SM00165A.
20. Hatte, S., and Pitchumani, R. (2022). Novel Nonwetting Solid-Infused Surfaces for Superior Fouling Mitigation. J. Colloid Interface Sci. *627*, 308–319. https://doi.org/10.1016/j.jcis.2022.06.155.
21. Pitchumani, R., and Stoddard, R. (2024). Solid-infused Surfaces, Articles Incorporating Solid-Infused Surfaces, Methods of Making, and Methods of Use Thereof. US Patent App. 18/559,525. https://patents.google.com/patent/US20240240036A1.
22. Hatte, S., Stoddard, R., and Pitchumani, R. (2023). Novel solid-infused durable nonwetting surfaces for sustained condensation heat transfer enhancement. Appl. Thermal Eng. *219*, 119458. https://doi.org/10.1016/j.applthermaleng.2022.119458.
23. Stoddard, R., Nithyanandam, K., and Pitchumani, R. (2022). Fabrication and Durability Characterization of Superhydrophobic and Lubricant-infused Surfaces. J. Colloid Interface Sci. *608*, 662–672. https://doi.org/10.1016/j.jcis.2021.09.099.
24. Miljkovic, N., Enright, R., and Wang, E.N. (2013). Modeling and optimization of superhydrophobic condensation. J. Heat Transfer *135*, 111004. https://doi.org/10.1115/1.4024597.
25. Rose, J.W. (1988). Some aspects of condensation heat transfer theory. Intern. Comm. Heat Mass Trans. *15*, 449–473. https://doi.org/10.1016/0735-1933(88)90043-7.
26. Rose, J.W. (2002). Dropwise condensation theory and experiment: A review. Proc. Inst. Mech. Eng. Part A J. Power Energy *216*, 115–128. https://doi.org/10.1243/09576500260049034.
27. Miljkovic, N., Enright, R., Nam, Y., Lopez, K., Dou, N., Sack, J., and Wang, E.N. (2013). Jumping-droplet-enhanced condensation on scalable superhydrophobic nanostructured surfaces. Nano Lett. *13*, 179–187. https://doi.org/10.1021/nl303835d.
28. Khatir, Z., Kubiak, K.J., Jimack, P.K., and Mathia, T.G. (2016). Dropwise condensation heat transfer process optimisation on superhydrophobic surfaces using a multi-disciplinary approach. Appl. Therm. Eng. *106*, 1337–1344. https://doi.org/10.1016/j.applthermaleng.2016.06.128.
29. Mandelbrot, B.B. (1985). Self-Affine Fractals and Fractal Dimension. Phys. Scr. *32*, 257.
30. Jain, R., and Pitchumani, R. (2017). Fractal Model for Wettability of Rough Surfaces. Langmuir *33*, 7181–7190. https://doi.org/10.1021/acs.langmuir.7b01524.
31. Majumdar, A., and Tien, C.L. (1991). Fractal network model for contact conductance. J. Heat Transfer *113*, 516–525. https://doi.org/10.1115/1.2910594.
32. Kim, S., and Kim, K.J. (2011). Dropwise condensation modeling suitable for superhydrophobic surfaces. J. Heat Transfer *133*, 1–8. https://doi.org/10.1115/1.4003742.
33. Nusselt, W. (1916). De oberflachenkondensation des waserdampfes. Z. VDI *541–546*, 569–575.
34. Kim, T., and Kim, S.J. (2024). Vertical-length effect on dropwise condensation heat transfer at low heat flux - Part I: Experimental study. Intern. J. Heat Mass Transf. *224*, 125329. https://doi.org/10.1016/j.ijheatmasstransfer.2024.125329.
35. Kim, T., and Kim, S.J. (2024). Vertical length effect on dropwise condensation heat transfer at low heat flux - Part II: Theoretical model suitable for non-coated metal surfaces. Intern. J. Heat Mass Trans. *226*, 125510. https://doi.org/10.1016/j.ijheatmasstransfer.2024.125510.
36. Gentoo Advanced Clear Hydrophobic Coating Technical Data Sheet (2021 (Ultratech International, Inc.), Rev 9 Sept. 2021. https://gentoocoating.com/tds.

STAR★METHODS

KEY RESOURCES TABLE

REAGENT or RESOURCE	SOURCE	IDENTIFIER
Chemicals, peptides and recombinant proteins		
Hydrochloric acid (12M)	Sigma Aldrich	Product no. 258148
Mercaptan	Sigma Aldrich	Product no. W389404
Margaric acid	Sigma Aldrich	Product no. H3500
Stearic acid	Sigma Aldrich	Product no. 175366
Gentoo	Thor Spill Products	https://www.thorspillproducts.com/products/ultra-tech-4700-gentoo-clear-hydrophobic-water-repelling-coating-quart-kit-part-a-b
Acetone	Sigma Aldrich	Product no. 179124
Methanol	Sigma Aldrich	Product no. 179337
Ethanol	Sigma Aldrich	Product no. 1.00986
Nitrogen gas	Sigma Aldrich	Product no. 295574
Software and algorithms		
Kaleidagraph	Synergy Software	https://www.synergy.com
LabView 2019	National Instruments	https://www.ni.com/en/shop/labview.html
Other		
Copper tube	McMaster Carr	Product no. 8967K89
Vacuum pump	Grainger	Product no. 406D57
Pressure gauge	Grainger	Product no. 54XP42
Pressure transducer	Grainger	Product no. 5LTF7
Borescope camera	Amazon	Dual-Lens Endoscope Camera with Light, DEPSTECH 1080P HD Borescope with 5″ IPS Screen, 16.5FT Flexible Sewer Camera, IP67 Waterproof Plumbing Snake Camera, Cool Gadgets for Men, Women: Amazon.com: Industrial & Scientific
Data acquisition (DAQ)	National Instruments	PXIe-6124
Resistance Temperature Detectors (RTD)	Grainger	Product no. 41A072
Flow meter	Omega	Product no. FTB-815-I
Chiller recirculator	Cole-Parmer	Product no. EW-20874-18
Immersion heater	Grainger	Product no. 2E931

METHOD DETAILS

Surface fabrication, characterization, and functionalization

As-purchased copper tubes with inner diameter of 8.7 mm and outer diameter of 9.5 mm were cleaned with acetone and deionized water before texturing. For multiscale rough texturing, either a process of electrodeposition or chemical etching was used. For etched samples, outer surface of the tubes was immersed in a bath of 12M hydrochloric acid for 20 min, whereas electrodeposited samples were prepared using a two-step electrodeposition process[14] at electrodeposition potential of either 0.7 V or 1.1 V. Both chemically etched and electrodeposited samples were imaged using a Zeiss 1550 field-emission scanning electron microscope and multiscale surface profiles were characterized using a Dektak XT stylus non-contact profilometer, from which fractal parameters were determined as explained in Figure 1.

For a variety of surface textures and wettability, chemically etched and electrodeposited samples were functionalized using three different functionalizing agents, namely, mercaptan, margaric acid and stearic acid. Functionalization of samples with mercaptan, margaric acid and stearic acid is similar in nature. Copper tube samples were subjected to 1-h immersion in 0.02 mol/L of the respective functionalizing agent at room temperature. The functionalized samples were removed from the immersion bath and rinsed with deionized water and methanol/ethanol, followed by drying with nitrogen gas.

Fabrication of solid-infused surfaces (SIS) started with the etched or electrodeposited rough surfaces as the first step. Following that, the roughened copper tube samples were then immersed in the bath of a two-part Gentoo polymer[36] for about 30 min. After removal, the Gentoo infused samples were spun at approximately 1700 rpm to remove the excess coating of the polymer. The samples were then air-dried at room temperature for about 10 min followed by curing at around 90 ° C for 1 h at atmospheric pressure. Gentoo is a nonwetting polymer initially in a liquid form with high density and affinity toward the metal surface.

Experimental methodology

A schematic of the experimental setup is shown in the supplemental information Section, where a 20 cm long single condenser tube with inner diameter of 8.7 mm and outer diameter of 9.5 mm was mounted inside an insulated vacuum chamber of dimensions 50cm × 35cm × 30cm. The outer surface of the condenser tube was textured to produce multiscale features by either electrodeposition or chemical etching, followed by functionalization with an appropriate agent. However, the inner surface of the tube was not textured or chemically altered. The condensation chamber was made of aluminum, insulated from outside to reduce heat loss to the ambient, and installed with a 1000 W immersion heater for steam generation. A vacuum chamber was installed with an adjustable vacuum pump to control pressure inside the chamber down to as low as 5 kPa. For coolant flow inside the copper tubes, a Cole-Parmer Polystat cooling/heating recirculator was used. Coolant flow inlet and outlet temperatures were measured using thermocouples, as depicted in the schematic. Additional thermocouples were installed inside the chamber to measure water and steam temperature. Data acquisition was done using National Instruments hardware and LabView 2019 software.

During condensation heat transfer experiments, the chamber was first filled partly with warm water at a temperature of around 40°C. At this stage, coolant recirculation at a relatively higher value was started to obtain a desired flow rate, and the vacuum pump was switched on to gradually reduce the chamber pressure to a value of about 8 kPa. Next, the immersion heater was switched on and water was allowed to boil for about 30 min to get rid of non-condensable gases. After this, as the chamber temperature and pressure were maintained at the desired values, the coolant inlet temperature was reduced to a desired stable value to mark the start of condensation process and coolant inlet/outlet, and chamber saturation temperatures were continuously measured at an interval of 0.5 s. Condensation images were taken with a top-mounted camera at desired stages of the experimental stages.

QUANTIFICATION AND STATISTICAL ANALYSIS

The quantification was carried out by calculating the mean (average) value from 20 measurements in each case. The statistical error in the measurement was calculated using population based standard deviation values. For reporting, a 95% confidence interval is chosen.